Bioactive Materials 34 (2024) 354–365

Contents lists available at ScienceDirect

Bioactive Materials

journal homepage: www.keaipublishing.com/en/journals/bioactive-materials

Intelligent nanoreactor coupling tumor microenvironment manipulation and H_2O_2-dependent photothermal-chemodynamic therapy for accurate treatment of primary and metastatic tumors

Jie Liu [a,1], Tianfeng Yang [b,1], Handan Zhang [a], Lin Weng [a], Xiuhong Peng [b], Tao Liu [a,c], Cheng Cheng [b], Yanmin Zhang [b,**], Xin Chen [a,*]

[a] School of Chemical Engineering and Technology, Shaanxi Key Laboratory of Energy Chemical Process Intensification, Institute of Polymer Science in Chemical Engineering, Xi'an Jiaotong University, Xi'an, 710049, China
[b] School of Pharmacy, Health Science Center, Xi'an Jiaotong University, Xi'an, 710061, China
[c] National & Local Joint Engineering Research Center of Biodiagnosis and Biotherapy, The Second Affiliated Hospital of Xi'an Jiaotong University, Xi'an, 710004, China

ARTICLE INFO

Keywords:
Nanoreactor
H_2O_2-dependent
Photothermal-chemodynamic therapy
Copper depletion
Tumor metastasis inhibition

ABSTRACT

Tumor microenvironment (TME), as the "soil" of tumor growth and metastasis, exhibits significant differences from normal physiological conditions. However, how to manipulate the distinctions to achieve the accurate therapy of primary and metastatic tumors is still a challenge. Herein, an innovative nanoreactor (AH@MBTF) is developed to utilize the apparent differences (copper concentration and H_2O_2 level) between tumor cells and normal cells to eliminate primary tumor based on H_2O_2-dependent photothermal-chemodynamic therapy and suppress metastatic tumor through copper complexation. This nanoreactor is constructed using functionalized MSN incorporating benzoyl thiourea (BTU), triphenylphosphine (TPP), and folic acid (FA), while being co-loaded with horseradish peroxidase (HRP) and its substrate ABTS. During therapy, the BTU moieties on AH@MBTF could capture excessive copper (highly correlated with tumor metastasis), presenting exceptional anti-metastasis activity. Simultaneously, the complexation between BTU and copper triggers the formation of cuprous ions, which further react with H_2O_2 to generate cytotoxic hydroxyl radical (•OH), inhibiting tumor growth via chemodynamic therapy. Additionally, the stepwise targeting of FA and TPP guides AH@MBTF to accurately accumulate in tumor mitochondria, containing abnormally high levels of H_2O_2. As a catalyst, HRP mediates the oxidation reaction between ABTS and H_2O_2 to yield activated ABTS•$^+$. Upon 808 nm laser irradiation, the activated ABTS•$^+$ performs tumor-specific photothermal therapy, achieving the ablation of primary tumor by raising the tissue temperature. Collectively, this intelligent nanoreactor possesses profound potential in inhibiting tumor progression and metastasis.

1. Introduction

Tumor microenvironment (TME) is a complex and heterogeneous collection of tumor cells, stromal cells, immune cells, blood vessels, and extracellular matrix, which has been recognized as the "soil" of tumor occurrence, growth, and metastasis [1–3]. Due to the disordered energy metabolism, hypoperfusion, uncontrolled cell growth, the physiological characteristics of TME are different from those of healthy tissue, including elevated copper, increased H_2O_2 concentration, and acidity [4,5]. However, developing a feasible method to utilize the differences between TME and normal physiological conditions for tumor treatment remains a problem.

As to overcome afore-mentioned challenge, new strategy such as photothermal therapy (PTT) has been introduced to combat against malignant tumors owing to its spatiotemporal controllability and noninvasive characteristic [6–8]. As a highly promising therapeutic manner of tumor, PTT could induce tumor cell apoptosis by raising the tissue temperature [9,10]. Even if it exhibits significant killing effect for

Peer review under responsibility of KeAi Communications Co., Ltd.
* Corresponding author.
** Corresponding author.
E-mail addresses: zhang2008@xjtu.edu.cn (Y. Zhang), chenx2015@xjtu.edu.cn (X. Chen).
[1] These authors contributed equally to this work.

https://doi.org/10.1016/j.bioactmat.2023.12.028
Received 28 September 2023; Received in revised form 23 December 2023; Accepted 29 December 2023

tumor cells, the conventional PTT still causes serious damage to surrounding healthy tissue because the photothermal transduction agents are randomly internalized by normal cells [11–13]. Therefore, it is greatly desirous to establish a selective PTT system based on the manipulation of TME for producing photothermal effects only in tumor cells.

In abnormal TME, excessive reactive oxygen species (ROS), particularly H_2O_2, offer a superior opportunity for selective PTT [14]. It is reported that the concentration of H_2O_2 in cancer cells (1×10^{-4} M) is much higher than that in normal cells (2×10^{-8} M) [15]. As a frequently-used indicator of H_2O_2, the horseradish peroxidase (HRP) could catalyze the conversion of 2,2′-azino-bis (3-ethylbenzothiazoline-6-sulfonic acid) (ABTS) to form ABTS•$^+$ in presence of high concentration of H_2O_2 [16,17]. Upon near-infrared (NIR) irradiation, the ABTS•$^+$ with strong NIR absorption displays excellent photothermal conversion efficiency [18]. Hence, the ABTS&HRP system is considerably appropriate to serve as a selective PTA.

Despite showing distinguished therapeutic effects on primary tumor, this PTT based on the ABTS&HRP system is incapable of suppressing the tumor metastasis, which is closely associated with a high mortality rate of tumors. Angiogenesis is considered as an indispensable step during the process of tumor metastasis [19]. In TME, the copper content is aberrantly elevated due to the reduced decomposition of ceruloplasmin [20–22]. The higher copper level can be conducive to the expression of pro-angiogenic factors, including vascular endothelial growth factor (VEGF) [23], fibroblast growth factor (FGF) and transforming growth factor-b (TGF-b) [24]. Consequently, copper depletion therapy could significantly enhance the anti-metastasis effect. Multitudinous copper-chelating agents have been employed to chelate additional copper *in vivo*, such as tetrathiomolybdate, D-penicillamine, acyl

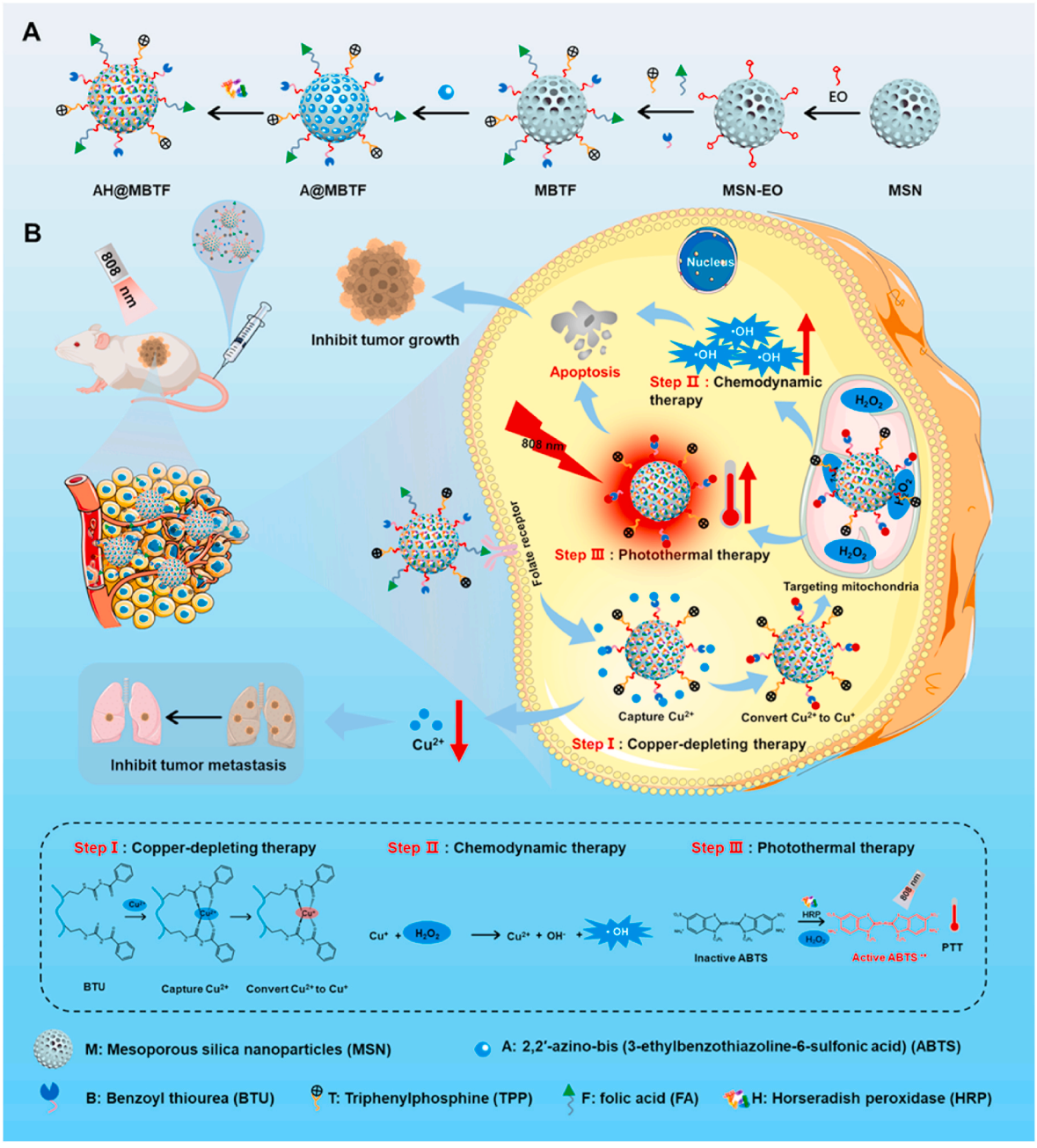

Scheme 1. Illustration of preparation (A) and therapeutic mechanism (B) of AH@MBTF nanoreactor for performing H_2O_2-responsive photothermal-chemodynamic therapy to eliminate primary tumor and chelating copper to inhibit metastatic tumor.

thiourea, and trientine hydrochloride [25,26]. Among them, thioureas groups could not only bind copper with a high stability constant, but also reduce Cu^{2+} to Cu^{+} [27,28]. It is well established that Cu^{+} catalyzes H_2O_2 in Fenton like reaction to generate cytotoxic hydroxyl radical (•OH) [29], which is an effective approach to devastate tumor cells [30].

Herein, we have designed a H_2O_2-responsive and multifunctional nanoreactor ($ABTS^{HRP}$@MSN-BTU-TPP-TA, AH@MBTF for short) for the inhibition of tumor growth and metastasis via regulating TME. To fabricate the nanoreactor, the mesoporous silica nanoparticles (MSN) are employed as nanocarriers to conjugate with folic acid (FA, active targeting group), triphenylphosphine (TPP, mitochondrial targeting molecule) [31–33], and benzoyl thiourea (BTU, copper ion chelator), and then loaded with ABTS&HRP. During therapy, the nanoreactor can actively accumulate to tumor cells with the assistance of FA. After internalization, the BTU segment would capture the excessive Cu^{2+} in tumor and convert Cu^{2+} to Cu^{+}. The copper depletion inhibits the ability of cancerous cells to invade and metastasize. Subsequently, TPP is in charge of guiding nanoreactor into tumor mitochondria with abundant H_2O_2 [34]. On one hand, the cytotoxic •OH based on the Fenton reaction between H_2O_2 and Cu^{+} was generated, further enhancing the antitumor effect. On the other hand, the HRP would catalyze the ABTS activation in the presence of sufficient H_2O_2. Upon laser radiation, the activated $ABTS^{•+}$ performed the tumor-specific PTT and minimizes the damage to normal tissues without abnormal accumulation of H_2O_2. Taking advantage of the H_2O_2-dependent photothermal-chemodynamic therapy and copper chelation, the nanoreactor is expected to completely ablate primary tumor and suppress metastatic tumor (Scheme 1).

2. Materials and methods

2.1. Synthesis of AH@MBTF

The loading of ABTS in MBTF was achieved by physical absorption, and 50 mg of MBTF was dispersed in 50 mL of mixed solution (1:1 of ethanol and water, v/v), followed by the addition of 100 mg of ABTS. The mixture was stirring for 24 h. The solution was centrifugated with DI water and then freeze-dried to get A@MBTF.

Firstly, 100 mg A@MBTF was dispersed in mixed solution (1:1 of ethanol and water, v/v) and 200 mg HRP was added. Then, the mixture was swirled and stirred for 24 h. The mixture was washed with DI water to remove free HRP and the AH@MBTF was obtained by freeze drying.

2.2. H_2O_2-dependent catalysis and photothermal effect

H_2O_2 was mixed with different formulations: AH@MBTF, A@MBTF, H@MBTF and MBTF. The HRP-mediated catalysis was estimated by the UV–Vis spectrums post-reaction at 0.5h and the photothermal effect of nanoreactor was evaluated by the variation of temperature. Then, the AH@MBTF was dispersed in 1 mL of solutions containing different pH and H_2O_2 (pH 7.4, H_2O_2: 10 nM; pH 6.8, H_2O_2: 100 μM; pH 8.0, H_2O_2: 10 mM). The UV–Vis absorbance and temperature change were recorded. *2.3. Cu^{2+} capture capability and ROS generation.*

The AH@MBTF was added in different ion solutions ($CuCl_2$, $CaCl_2$, $MgCl_2$, and $MnCl_2$) for stirring 24 h. The mixture solutions were digested with dilute nitric acid and the ion concentration was measured by atomic absorption spectrum. As a Cu^{+}-specific sequestering agent, BCS was employed to characterize the transformation process from Cu^{2+} to Cu^{+}. In brief, AH@MBTF was incubated with $CuCl_2$ solution for 0.5h, and then the BCS was added in the solution. After 10min, the absorption spectrum was measured. For ROS formation, the mixed solution containing AH@MBTF, H_2O_2, and $CuCl_2$ was prepared. After 0.5 h reaction, TMB solution was dispersed in the solution and the sample was detected using UV–Vis spectrophotometer.

2.3. Reactive oxygen species detection

DCFH-DA reagent was applied to evaluate the intracellular ROS levels. In brief, 4T1 cells were seeded into 6-well plates for 24 h incubation. After removing medium, the cells were co-cultures with PBS, AH@MTF, AH@MBTF, AH@MBF, AH@MBTF+L for 48 h. After that, the cells were rinsed by PBS and stained with DCFH-DA solution (10 μM) for 30 min in the dark. After the cells are harvested, the fluorescence intensity of DCFH-DA was analyzed by flow cytometer.

2.4. MTT assay

The cytotoxicity of NPs and was estimated with 4T1 cells and MCF-10A cells via MTT assay. Briefly, cells were plated into 96-well plates and cultured for overnight. Then, the cells were treated with PBS, AH@MTF, AH@MBTF, AH@MTF+L, AH@MBTF, AH@MBTF+L, and AH@MBF+L. After incubation for 48 h, the fresh medium containing MTT (5 mg/ml) was cocultured with cells for additional 4 h. Subsequently, the cell medium was replaced with 150 μl of DMSO and the plates were shaken for 15 min. The absorbance of cells at 490 nm was analyzed with a Bio-Rad microplate reader and the cell viability was calculated according to the standard formula.

2.5. Mitochondrial membrane potential (ΔΨm) assay

The dysfunction of mitochondria could be evaluated by the decline of ΔΨm and JC-1 is an ideal fluorescence probe for detecting ΔΨm. The 4T1 cells were cultured into a 6-well plate and given different treatments of PBS, AH@MTF, AH@MBTF, AH@MTF+L, AH@MBTF, AH@MBTF+L, and AH@MBF+L for 24h. The harvested cells were performed the protocol of MitoProbe JC-1 Assay Kit and then analyzed by flow cytometry.

2.6. Apoptosis assay

The apoptosis efficacy of NPs was performed by Annexin V-FITC/PI apoptosis detection kit. 4T1 cells were seeded into a 6-well plate at 37 °C in 5 % CO_2, following by incubated with PBS, AH@MTF, AH@MBTF, AH@MTF+L, AH@MBTF, AH@MBTF+L, and AH@MBF+L for 24h. After washed with PBS, the cells were stained with Annexin V-FITC and PI for 15 min, sequentially. The cells were collected for flow cytometry analysis.

2.7. In vivo biodistribution and photothermal effects study

When the tumor volume was approximately 300 mm^3, the 4T1 tumor-bearing mice were intravenously injected with the AH^{D}@MBTF. The biodistribution of whole body was assessed by the *in vivo* imaging system at predetermined time intervals. The mice were sacrificed and the main tissues (heart, liver, spleen, lung, kidney, and tumor) were gained to detect the fluorescence signals at a preset time.

The photothermal conversion of nanoreactor was evaluated on the 4T1 Subcutaneous tumor model. The mice were administrated by intravenous injection of PBS and AH@MBTF once the tumor size reached 300 mm^3. At 48 h post-injection, 808 nm laser with a power of 1.25 W/cm^2 was utilized to irradiate the mice for 10 min. Before and after radiation, the thermal images of mice were recorded.

2.8. In vivo therapeutic efficacy study

The 4T1 tumor-bearing mice were randomly divided into five groups: PBS, AH@MTF+L, AH@MBF+L, AH@MBTF, and AH@MBTF+L. The mice (initial tumor volume: 50–100 mm^3), were intravenously administrated the formulations on day 0. The 808 nm laser irradiation (1.25 W/cm^2, 10 min) was conducted at 48 h post-injection. During the 21 days observation period, the tumor volume

and body weight were monitored every 2 days. At the end of the treatments, the mice were sacrificed and the tumors were collected for H&E, TUNEL, Ki67, and CD34 staining. The ROS level of tumor was detected with flow cytometry analysis. The survival rate curves of mice were assessed using Kaplan–Meier method and observed for 35 days. For anti-metastasis evaluation, the mice were euthanized and the lungs were soaked in Bouin's solution. After 4 h, the lung tissues were photographed and weighted. Besides, surface yellow nodules were counted and the tissues were performed the H&E, Ki67, and N-cadherin staining.

2.9. Statistical analysis

Data analysis was performed using GraphPad Prism version 7 software. All numerical values were expressed as the mean ± SD. For multiple comparisons, statistical analysis was performed using one-way analysis of variance (ANOVA) followed by a Bonferroni post-test. All significant values were indicated as follows: (*$p < 0.05$, **$p < 0.01$, ***$p < 0.001$; ns, no significance).

3. Results and discussion

3.1. Preparation and characterization of AH@MBTF

The AH@MBTF nanoreactor was based on MSN prepared by CTAB-templated method [35,36], which was further grafted with three functional groups (BTU, TPP, and FA) and loading with ABTS and HRP. To prepare AH@MBTF nanoreactor, BTU and TPP-NH_2 were firstly synthesized (Fig. S1A and Fig. S2A), which were verified by the Fourier transform infrared spectrometer (FT-IR) and ^{1}H nuclear magnetic resonance (^{1}H NMR) spectrum. The results (Figs. S1B and C), showed the characteristic vibrations and proton signals of C–H and N–H from ethylenediamine, suggesting the successful preparation of BTU. The synthesis of TPP-NH_2 were proved by the appearance of phenyl and amino in FT-IR and ^{1}H NMR spectrum of TPP-NH_2 (Figs. S2B and C).

The stepwise preparation procedure of MBTF (MSN-BTU/TPP/FA) was confirmed by FT-IR spectrum (Fig. 1A), which showed clear characteristic vibrations of Si–*O*–Si from MSN, C–C from TPP, C═N from FA, and C═S from BTU. Zeta potential change from MSN to AH@MBTF (Fig. S3A) further supported the gratifying preparation, which presented the surface charge transition of the functional groups as expected. Based on the differential thermal gravity analysis (DTG, Fig. S3B) of MBTF, the coupling of characteristic thermal signals of MSN-BTU, MSN-TPP, and MSN- FA was observed. According to the analysis of C peak from X-ray photoelectron spectroscopy (XPS) spectra of MBTF (Fig. 1B), C═S, C═N, and π bond from phenyl were respectively assigned to BTU, FA, and TPP, further indicating the successful modification of functional groups. The chemical composition of MBTF was investigated by energy dispersive spectroscopy (EDS) (Fig. 1C), which presented the typical characteristic elements of N, P, and S. The mapping images clearly revealed the homogeneous distribution of Si, O, N, P, and S (Fig. 1D), indicating the formation of MBTF. As shown in Fig. 1E, the resulting MBTF carrier exhibited a diameter around 190 nm with spherical morphologies. The large-scale TME image of MBTF was displayed in Fig. S4.

To obtain the catalytic nanoreactor, ABTS and HRP were

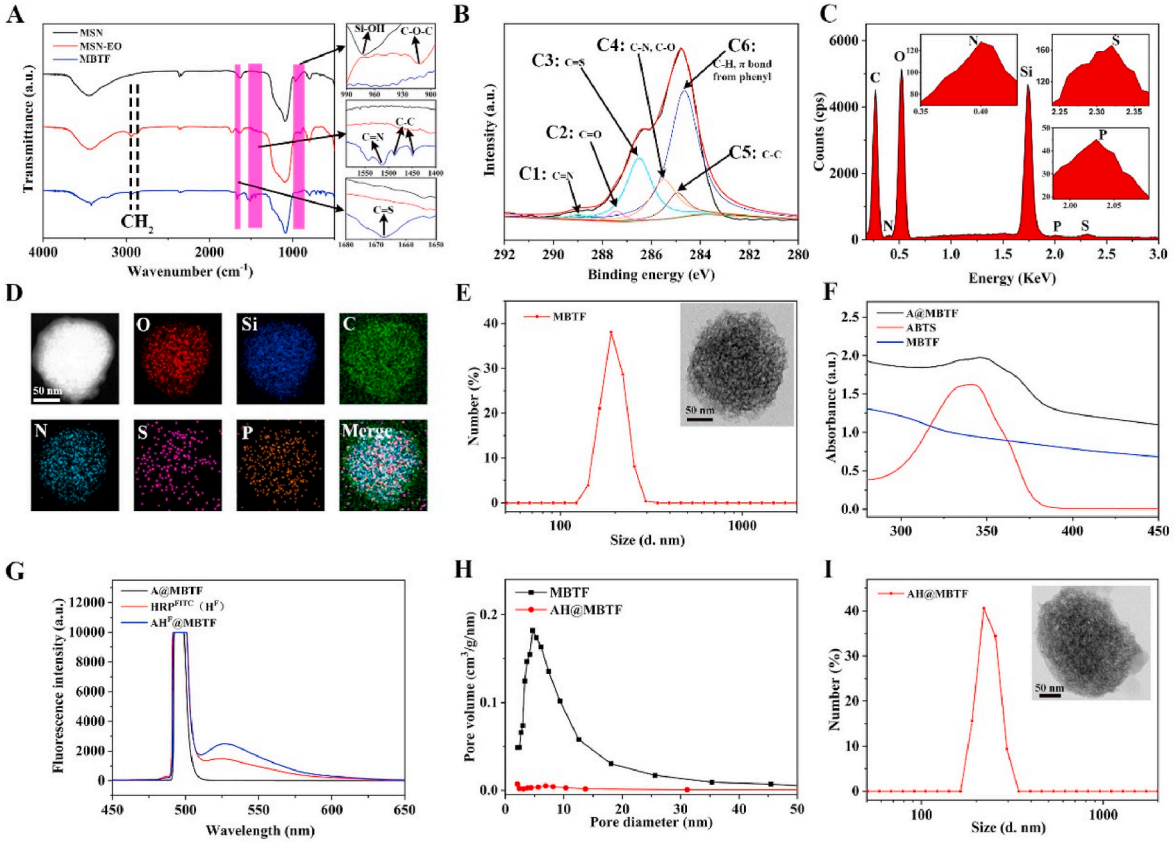

Fig. 1. A) Fourier transform infrared (FTIR) spectra of MSN, MSN-EO, and MBTF, characterizing the stepwise synthesis of functionalized MSN carrier. B) XPS survey spectrum of C 1s of MBTF. C) Energy-dispersive X-ray (EDX) spectroscopy of MBTF, confirming the elemental distribution. D) Mapping images of MBTF. E) Dynamic light scattering (DLS) measurements and TEM image (inset) of MBTF. F) The UV–Vis absorption spectra of A@MBTF, ABTS, and MBTF, demonstrating the Successful encapsulation of ABTS. G) Fluorescence spectra of A@MBTF, HRP^{FITC} (H^F), and AH^F@MBTF, indicating that HRP was loaded on functionalized MSN carrier. HRP was labeled with FITC. H) Pore size distribution of MBTF and AH@MBTF. I) DLS particle size distribution and TME image of AH@MBTF. MBTF represents the MSN-BTU/TPP/FA; A@MBTF represents the ABTS@MSN-BTU/TPP/FA; AH^F@MBTF represents the $ABTS^{FITC-HRP}$@MSN-BTU/TPP/FA; AH@MBTF represents the $ABTS^{HRP}$@MSN-BTU/TPP/FA.

successively loaded on the MBTF carrier. The UV–vis spectrum of A@MBTF (ABTS@MSN-BTU/TPP/FA) presented the characteristic absorption peak of ABTS at 342 nm, demonstrating that ABTS was encapsulated in the pores of carrier as expected (Fig. 1F). Fluorescein isothiocyanate (FITC) was utilized to label HRP for verification the loading of HRP. As shown in Fig. 1G, the characteristic emission peak of FITC at 520 nm was observed in the fluorescence spectrum of AH^{F}@MBTF ($ABTS^{HRP\text{-}FITC}$@MSN-BTU/TPP/FA), which was similar with that of HRP^{FITC}, suggesting the successful loading of HRP. The absorbance of ABTS (Fig. S5A) and the fluorescence intensity of HRP^{FITC} (Fig. S5D) maintained an obvious linear dependence with the concentration of ABTS and HRP^{FITC}, separately. Based on the standard curves of ABTS (Fig. S5B) and HRP^{FITC} (Fig. S5E), the loading rates of ABTS and HRP were determined to be 6.67 % (Fig. S5C) and 1.25 % (Fig. S5F), respectively. In addition, the mesoporous structure of AH@MBTF almost disappeared, further indicating that ABTS and HRP were successfully loaded into the pores of MSN (Fig. 1H). The release rates of ABTS and HRP were quite low under different pH conditions, demonstrating the satisfactory stability of AH@MBTF (Figs. S6A and B). The final AH@MBTF nanoreactor had a slightly increased size particle of around 210 nm and a spherical morphology attached by organic layer (Fig. 1I). The TEM image of AH@MBTF with multiple particles was presented in Fig. S7.

3.2. Response performance studies of AH@MBTF in vitro

In the case of excessive H_2O_2 in tumor, inactive ABTS could be oxidized by HRP to form activated $ABTS\bullet^{+}$, which displays the strong NIR absorption and delightful photothermal effect for tumor tissue. Next, the enzyme-catalyzed behavior of AH@MBTF was investigated. The UV–Vis absorption spectra of AH@MBTF+H_2O_2 exhibted obvious triple absorption peaks of $ABTS\bullet^{+}$ between 600 and 900 nm, which was consistent with that of free ABTS+HRP+H_2O_2 (Fig. 2A). In view of the strong absorption of $ABTS\bullet^{+}$ in the NIR region, the AH@MBTF+H_2O_2 and free ABTS+HRP+H_2O_2 presented the similar temperature rise after NIR radiation (Fig. 2B), reflecting that the photothermal ability of AH@MBTF indeed came from the HRP catalyzed ABTS conversion under the condition of H_2O_2. In addition, the AH@MBTF nanoreactor still maintained satisfactory photothermal stability even after four laser switching on/off cycles (Fig. S8). PBS solutions containing different pH and various concentrations of H_2O_2 were applied to simulate different physiological environments: normal tissue (pH = 7.4, [H_2O_2] = 10 nM),

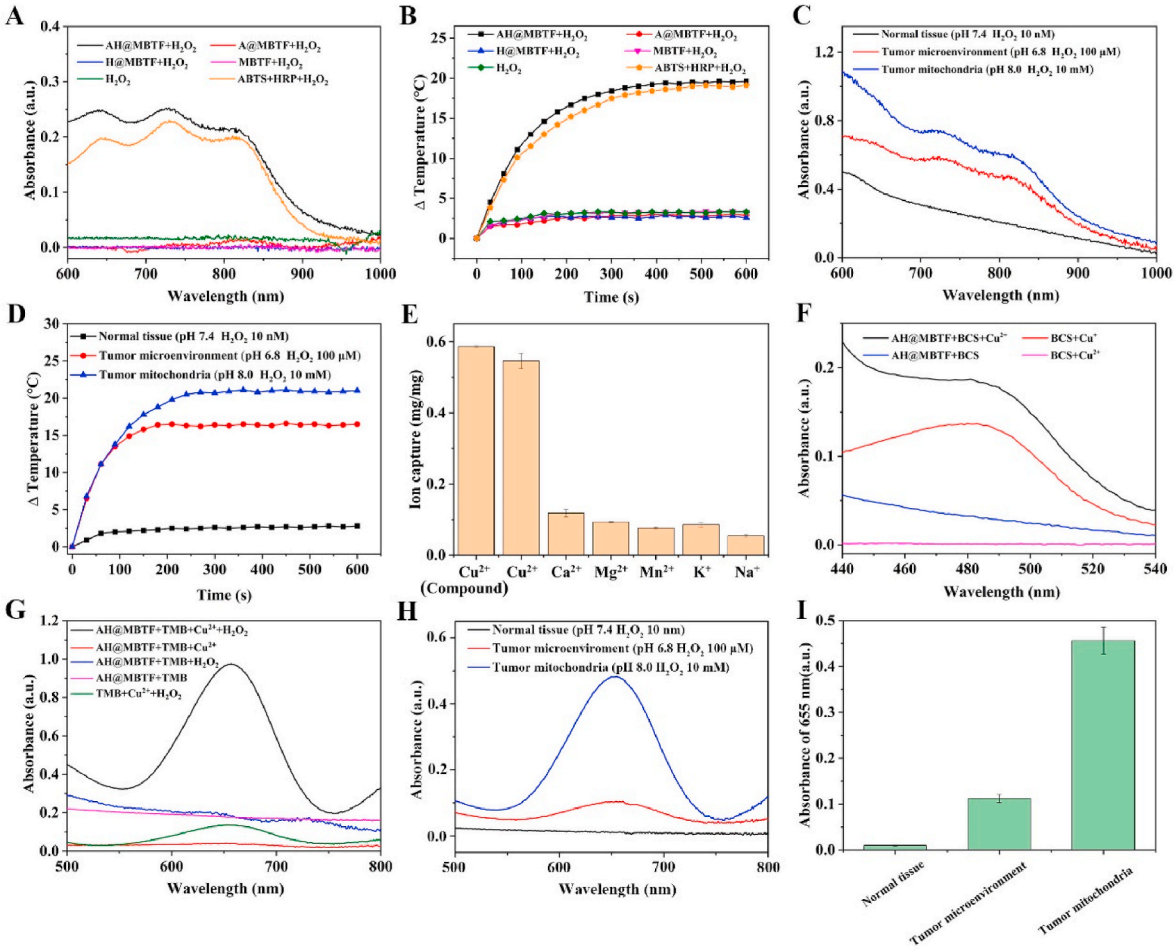

Fig. 2. A) Ultraviolet–visible (UV–Vis) and B) temperature-changing curve of AH@MBTF+ H_2O_2, A@MBTF+ H_2O_2, H@MBTF+H_2O_2, MBTF+H_2O_2, H_2O_2, and ABTS+HRP+ H_2O_2. C) UV–vis spectrum and D) photothermal curves of AH@MBTF under different conditions, including simulated normal tissue, tumor microenvironment, and tumor mitochondria. E) Ion capture property of AH@MBTF in different aqueous solutions containing Cu^{2+}, Ca^{2+}, Mg^{2+}, Mn^{2+}, K^{+}, Na^{+} or mixed ions, which were detected by atomic absorption spectrum. F) UV–vis spectrum of AH@MBTF+BCS+Cu^{2+}, AH@MBTF+BCS, BCS+Cu^{2+}, and BCS+Cu^{+}, indicating the reduction of Cu^{2+} to Cu^{+} detected by BSC. G) The ROS generation via the Fenton reaction between the formed Cu^{+} and H_2O_2 by TMB detection. The absorbance spectrum of AH@MBTF+TMB+Cu^{2+}+H_2O_2, AH@MBTF+TMB+Cu^{2+}, AH@MBTF+TMB+ H_2O_2, AH@MBTF+TMB, and TMB+ Cu^{2+}+H_2O_2. H) The ROS formation of AH@MBTF in simulated physiological environments detected by TMB. I) Statistics of the absorbance at 655 nm of AH@MBTF+TMB in different environments. MBTF represents the MSN-BTU/TPP/FA; A@MBTF represents the ABTS@MSN-BTU/TPP/FA; H@MBTF represents the HRP@MSN-BTU/TPP/FA; AH@MBTF represents the $ABTS^{HRP}$@MSN-BTU/TPP/FA.

tumor microenvironment (pH = 6.8, [H_2O_2] = 100 μM), and tumor mitochondria (pH = 8.0, [H_2O_2] = 10 mM). Compared with the negligible absorbance spectrum and temperature change in normal tissue, AH@MBTF in tumor mitochondria displayed stronger triple absorption in NIR spectrum and superior photothermal conversion efficiency (Fig. 2C and D). In addition, the effect of different H_2O_2 concentrations or pH on photothermal properties was studied. As the H_2O_2 concentration increased, the absorbance of AH@MBTF at NIR region was dramatically enhanced and the temperature was significantly elevated (Figs. S9A and B). However, the variation of pH did not bring about the change of NIR absorption spectrum and photothermal property (Figs. S9C and D). These results convincingly demonstrated that the AH@MBTF nanoreactor could serve as an outstanding photothermic agent in the subsequent precise treatment of tumor.

The thiourea groups of BTU exert strong copper-chelation capability, which provides favorable support to deplete the excessive copper in tumor. At first, the copper selective complexation of AH@MBTF nanoreactor was explored in PBS containing various common microelement ions. It can be seen from Fig. 2E, the AH@MBTF showed highly selective capture of Cu^{2+} far over other common microelement ions (Na^+, K^+, Mn^{2+}, Mg^{2+}, and Ca^{2+}), which was conducive to regulate the Cu^{2+} level in tumor microenvironment. Additionally, the complexation between

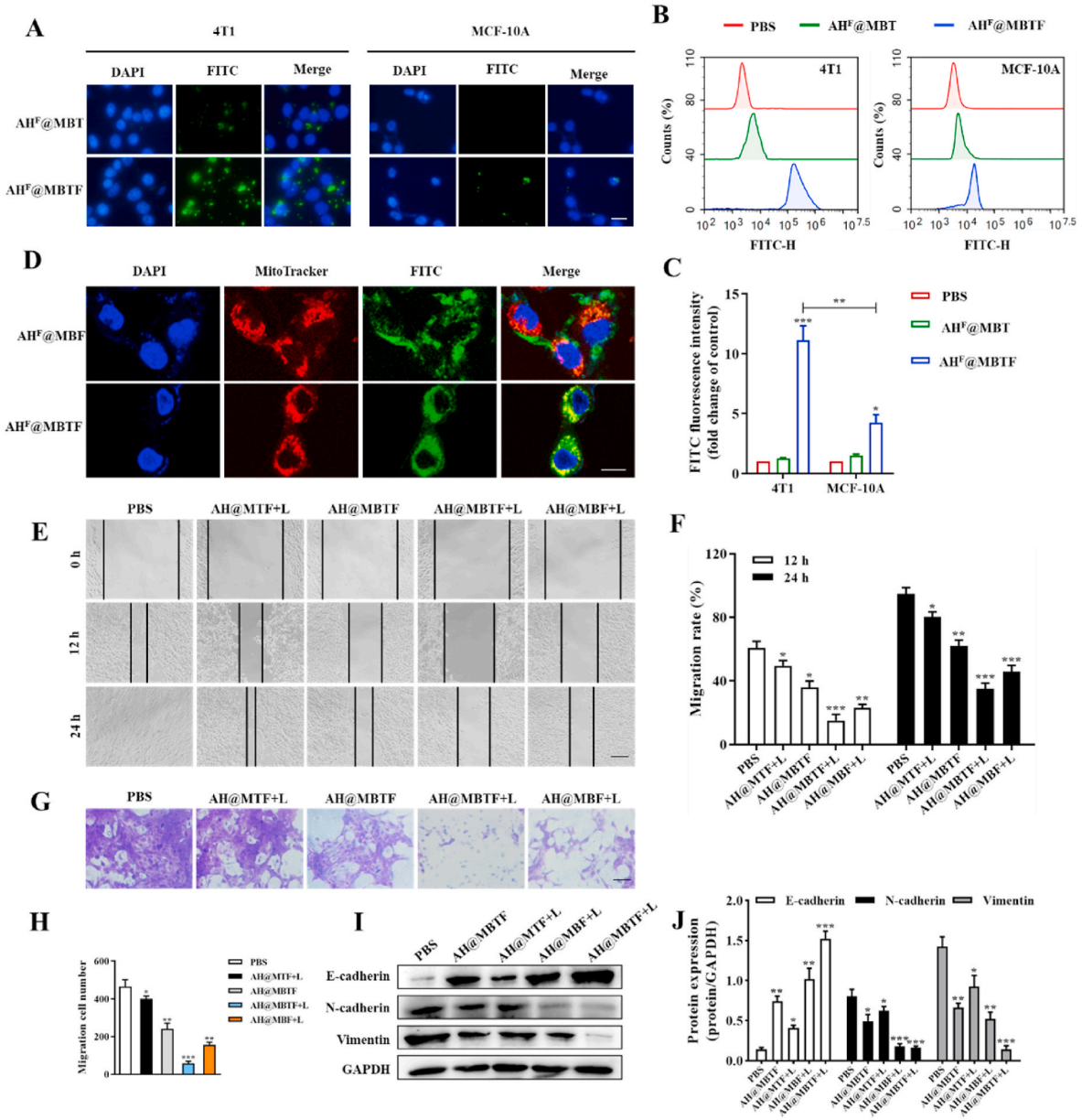

Fig. 3. A) Fluorescent microscope images of 4T1 cells and MCF-10A cells after incubation with AH^F@MBT and AH^F@MBTF for 24 h. B) flow cytometry and representative quantitative analysis C) of 4T1 cells and MCF-10A cells after 24 h co-incubation with PBS, AH^F@MBT and AH^F@MBTF. D) Confocal fluorescence images of 4T1 cells after incubated with AH^F@MBF and AH^F@MBTF. The nucleus and mitochondria were stained by blue and red fluorescent, respectively. E) Wound healing assay and F) quantitative analysis of different formulations: PBS, AH@MTF+L, AH@MBTF, AH@MBTF+L, and AH@MBF+L. G) Transwell invasion assay and H) quantitative analysis of 4T1 cells incubated with various treatments. I) Transfer factors expression (E-cadherin, N-cadherin and Vimentin) and J) quantitative analysis of 4T1 cells after treatment with various formulations. AH^F@MBT represents the $ABTS^{FITC-HRP}$@MSN-BTU/TPP; AH^F@MBTF represents the $ABTS^{FITC-HRP}$@MSN-BTU/TPP/FA; AH^F@MBF represents the $ABTS^{FITC-HRP}$@MSN-BTU/FA; AH@MTF+L represents the $ABTS^{HRP}$@MSN- TPP/FA with 808 nm laser irradiation; AH@MBTF represents the $ABTS^{HRP}$@MSN-BTU/TPP/FA; AH@MBTF+L represents the $ABTS^{HRP}$@MSN-BTU/TPP/FA with 808 nm laser irradiation; AH@MBF+L represents the $ABTS^{HRP}$@MSN-BTU/FA with 808 nm laser irradiation. The scale bar is 20 μm *$p < 0.05$, **$p < 0.01$ and ***$p < 0.001$ versus PBS group.

BTU and Cu^{2+} involved the formation of Cu^{+}. As a specific complexant of Cu^{+}, bathocuproine disulfonate (BCS) was utilized to detect the generation of Cu^{+} [37,38]. After adding BCS to the AH@MBTF/$CuCl_2$ solution, the appearance of characteristic absorption at 480 nm revealed the formation of Cu^{+} (Fig. 2F). To further determine the state between Cu^{+} and nanoreactor, XPS was used to investigate the AH@MBTF after mixing with Cu^{2+}. As can be seen from Fig. S10, the XPS spectra of Cu 2p exhibited the peaks of Cu^{+}-S at 931.91 eV and Cu^{+}-O at 934.2 eV, indicating the formation of complex between Cu^{+} and AH@MBTF [27,39–41]. Moreover, Fig. S11, the residula content of Cu in the AH@MBTF-Cu complex maintained well at 99.8 % even after 48 h incubation, and no visible diffusion of the copper ions appeared until the end of incubation, performing a high stability in PBS (Fig. S11). These results indicated that all the copper captured by AH@MBTF existed as the state of stable complex. In addition, the obtained Cu^{+} could react with excessive H_2O_2 of tumor tissue to produce •OH, which was considered as the most toxic ROS. 3,3′,5,5′-tetramethyl-benzidine (TMB) has been explored as a feasible chromogenic agent for •OH detection. As seen from Fig. 2G, the characteristic absorption peak at 655 nm was observed when TMB was added to the mixed solution of AH@MBTF, $CuCl_2$, and H_2O_2, suggesting the emergence of •OH. As expected, AH@MBTF in the tumor mitochondria generated a large amount of •OH, which was demonstrated by the intense absorption of 655 nm (Fig. 2H and I).

3.3. In vitro tumor therapy of AH@MBTF

To further evaluate the cancer therapeutic efficacy, the selective cellular uptake of AH@MBTF was first investigated by fluorescence microscopy and flow cytometry. FITC labeled HRP was employed to track the nanoreactor (AH^{F}@MBTF). The 4T1 cells and MCF-10A cells were selected as the model tumor cells and normal cells, respectively. As shown in Fig. 3A, AH^{F}@MBTF displayed the strong fluorescence signal of FITC in 4T1 cells, whereas only weak fluorescence signal was observed in AH^{F}@MBT ($ABTS^{FITC-HRP}$@MSN-BTU/TPP), indicating that FA as an active targeting group could promote the tumor cellular uptake of the nanoreactor. Meanwhile, there was no noteworthy fluorescence signal of AH^{F}@MBTF and AH^{F}@MBT in MCF-10A cells. Moreover, the results of flow cytometry analysis further revealed that the uptake efficiency of AH^{F}@MBTF in 4T1 cells was much stronger than that in MCF-10A cells (Fig. 3B and C). The tumor mitochondria were labeled with MitoTracker to detect whether the nanoreactor could specifically accumulate in mitochondria. In the absence of TPP, the green fluorescence of AH^{F}@MBF ($ABTS^{FITC-HRP}$@MSN-BTU/FA) was not overlapped with the red signal of mitochondria (Fig. 3D). However, AH^{F}@MBTF (green fluorescence) co-localized well with mitochondria (red fluorescence), verifying that the introduction of TPP endowed AH^{F}@MBTF with the active targeting ability to mitochondria.

On view of the promoting effect of copper during tumor metastasis, AH@MBTF was expected to suppress the metastasis of tumor cells via the copper complexation of BTU groups. Therefore, the inhibitory effects of AH@MBTF on 4T1 cells migration and invasion were evaluated by wound healing and transwell migration assay, respectively. As indicated in Fig. 3E and **F**, the AH@MTF+L group ($ABTS^{HRP}$@MSN-TPP/FA with 808 nm laser irradiation, without BTU) exhibited a minor anti-migratory effect, while the wound healing was clearly hindered in AH@MBTF group due to the copper complexation of BTU. With the 808 nm irradiation, the lowest efficiency of 4T1 cells migration was noticed in AH@MBTF+L group ($ABTS^{HRP}$@MSN-BTU/TPP/FA with 808 nm laser irradiation), which was attributed to the decreased cell activity induced by photothermal effect and ROS generation. The anti-migratory effect of AH@MBF+L group ($ABTS^{HRP}$@MSN-BTU/FA with 808 nm laser irradiation, without TPP) was slightly lower than that of AH@MBTF+L group because the lack of mitochondrial targeting function led to a reduction in ROS content. With treatment time from 12 h to 24 h, the afore-mentioned trends of migration inhibition against 4T1 cells were more obvious. Furthermore, the inhibitory effect of nanoreactor on the 4T1 cells invasiveness was assessed. Consistent with the results of wound healing assay, the AH@MBTF group could more significantly attenuate the invasion of tumor cells relative to the AH@MTF+L group, which was benefited from presence of BTU (Fig. 3G and H). The AH@MBTF+L group still maintained the strongest invasion-resistant ability. Epithelial-mesenchymal transition (EMT) was considered as the indispensable role in tumor metastasis [42]. To further examine whether the nanoreactor inhibited 4T1 cells metastasis by acting on EMT, the marker proteins (E-cadherin, N-cadherin and Vimentin) of EMT progression were detected by western blotting. The E-cadherin expression is negatively correlative with EMT, yet the expressions of N-cadherin and vimentin are positively correlative with EMT. Apparently, in the AH@MBTF+L group, E-cadherin was most significantly up-regulated, while the N-cadherin and vimentin were most remarkably down-regulated (Fig. 3I, **J**). The result demonstrated that the AH@MBTF nanoreactor could inhibit tumor metastasis via obstructing the EMT process. This process was attributed to the copper deficiency mediated inactivation of HIF-1α and down-regulation of hypoxia-associated transcription factors (Snail and Twist-1), which resulted in the dysregulation of EMT-related proteins [43].

As proved in the solution sample, AH@MBTF could reduce of Cu^{2+} to Cu^{+}, which further reacted with H_2O_2 to produce cytotoxic •OH. Thus, the intracellular ROS level was detected by flow cytometry with dichlorodihydrofluorescein diacetate (DCFH-DA) as a fluorescent probe [44]. As shown in Fig. 4A and B, the increase of intracellular ROS level in AH@MTF group ($ABTS^{HRP}$@MSN-TPP/FA) was negligible. With the introduction of BTU functional group, the Fenton reaction between Cu^{+} and H_2O_2 promoted the generation of ROS in AH@MBF ($ABTS^{HRP}$@MSN-BTU/FA)-treated cells. The further accumulation of ROS was observed in AH@MBTF (with TPP group), which was ascribed to the more adequate H_2O_2 from tumor mitochondrion. Moreover, the additional 808 nm radiation greatly improved the generation of ROS from AH@MBTF+L group owing to the more active Fenton reaction promoted by rising temperature. In addition, the intracellular •OH level was further detected by using the specific •OH-sensitive probe (BBox-iProbe®O26) [45–47]. As can be seen from Fig. S12, the most •OH was generated in the AH@MBTF with NIR radiation group owing to the enhancement of Fenton-like reaction under higher temperature, which was consistent with that of DCFH-DA. According to the above two studies, it can be concluded that our nanoreactor can perform the excellent chemodynamic effect. Subsequently, the efficacy of AH@MBTF for tumor photothermal therapy and chemodynamic therapy was tested by MTT assay. The copper plunder group (AH@MBTF) and photothermal treatment group (AH@MTF+L) displayed remarkable cytotoxicity against 4T1 cells (Fig. 4C). As expected, the 4T1 cells viability in multifunctional AH@MBTF+L group was tremendously suppressed because of the synergistic effect of copper chelation, mitochondrial targeting ability, PTT, and chemo-dynamic therapy. All treatment groups had no effect on the MCF-10A cells proliferation, indicating the good biocompatibility of AH@MBTF.

The cell apoptosis assay of AH@MBT was performed by annexin V–FITC/propidium iodide (PI) apoptosis detection kit. In accordance with the results of detection, AH@MBTF and AH@MTF+L could efficiently induce 54.70 % and 49.65 % cell apoptosis, respectively (Fig. 4D). Meanwhile, the largest apoptosis ratio of about 85.81 % appeared in AH@MBTF+L group due to the synergistic therapeutic effects (Fig. 4F). Since these formulations exerted main therapeutic effects in tumor mitochondria, the decline of mitochondrial membrane potential (ΔΨm), as one of the hallmark events of mitochondrial dysfunction, was assessed with a membrane-permeable JC-1 dye [48]. As determined by flow cytometry in Fig. 4E and **G**, after AH@MBTF treatment, the ΔΨm significantly decreased by 33.57 % versus the PBS group. With the addition of 808 nm radiation, the loss ratio of ΔΨm in AH@MBTF+L was up to 74.69 %, demonstrating the severe damaging of mitochondria by the synergistic effects. Once mitochondrial targeting ability was lost,

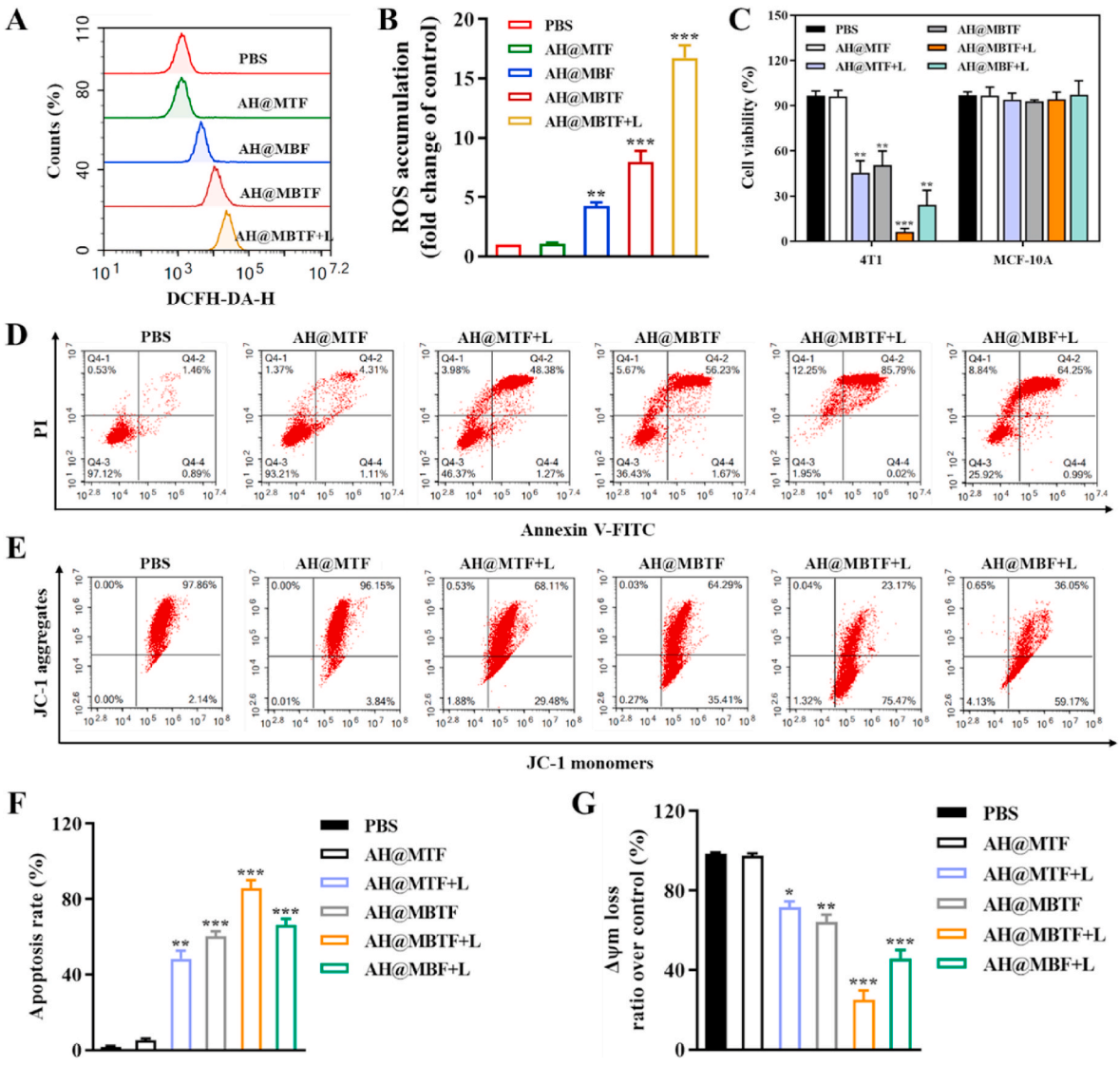

Fig. 4. A) ROS level of 4T1 cells after treatment with PBS, AH@MTF, AH@MBF, AH@MBTF, and AH@MBTF+L. B) Quantitative analysis of ROS accumulation relative to control group. C) Cell viability of 4T1 cells treated with PBS, AH@MTF, AH@MTF+L, AH@MBTF, AH@MBTF+L, and AH@MBF+L for 24h. D) Cell apoptosis and F) statistical analysis of 4T1 cells after different treatments. E) The change of mitochondrial membrane potential (ΔΨm) and quantitative analysis G) in 4T1 cells after treatments by different formulations. AH@MTF represents the $ABTS^{HRP}$@MSN-TPP/FA; AH@MBF represents the $ABTS^{HRP}$@MSN-BTU/FA; AH@MBTF represents the $ABTS^{HRP}$@MSN-BTU/TPP/FA; AH@MBTF+L represents the $ABTS^{HRP}$@MSN-BTU/TPP/FA with 808 nm laser irradiation; AH@MTF+L represents the $ABTS^{HRP}$@MSN-TPP/FA with 808 nm laser irradiation; AH@MBF+L represents the $ABTS^{HRP}$@MSN-BTU/FA with 808 nm laser irradiation. $^{*}p < 0.05$, $^{**}p < 0.01$ and $^{***}p < 0.001$ versus PBS group.

the situation of mitochondrial dysfunction in AH@MBF+L was weaker than that in AH@MBTF+L.

3.4. *In vivo* anti-tumor performance of AH@MBTF

Inspired by the promising anti-tumor performance *in vitro*, the therapeutic efficacy of AH@MBTF nanoreactor was evaluated by 4T1 tumor-bearing nude mice. The biodistribution of AH@MBTF was tested by using DiR as a fluorescent probe and shown in Fig. 5A. Apparently, the DiR-labeled AH@MBTF (AH^{D}@MBTF, $ABTS^{DiR-HRP}$@MSN-BTU/TPP/FA, AH^{D}@MBTF for short) gradually accumulated to tumor tissue in a time-dependent manner and the fluorescence intensity of DiR was still strong even at 48 h after injection. At every predetermined time point, the isolated organs and tumor tissue were harvested to detect the distribution of AH^{D}@MBTF in different organs. At the beginning, the nanoreactor mainly detained in liver owing to first pass elimination. As time elapsed, the rapid metabolism of AH^{D}@MBTF brought about less and less DiR fluorescence in liver. Conversely, the fluorescence signals in tumor regions continuously enhanced and shown a long residence time, which was advantageous for effective tumor treatment. The quantitative analysis of DiR fluorescence in tumor site was consistent with the result of biodistribution (Fig. S13). Next, the photothermal effect of AH@MBTF *in vivo* was carried out with laser irradiation. In contrary to the negligible temperature rise in PBS, the AH@MBTF exhibited a rapid temperature increase after irradiation for 10 min, suggesting the excellent photothermal effect (Fig. 5B).

After confirming the higher tumor accumulation capability and preeminent photothermal property, the *in vivo* antitumor efficacy of AH@MBTF was assessed using 4T1 tumor model. When the tumor volume reached 50–100 mm^3, the tumor-bearing mice were randomly divided into five groups: PBS, AH@MTF+L (photothermal therapy), AH@MBF+L (copper-depleting therapy, photothermal therapy, and chemo-dynamic therapy), AH@MBTF (copper-depleting therapy, chemo-dynamic therapy, and mitochondrial targeting), and

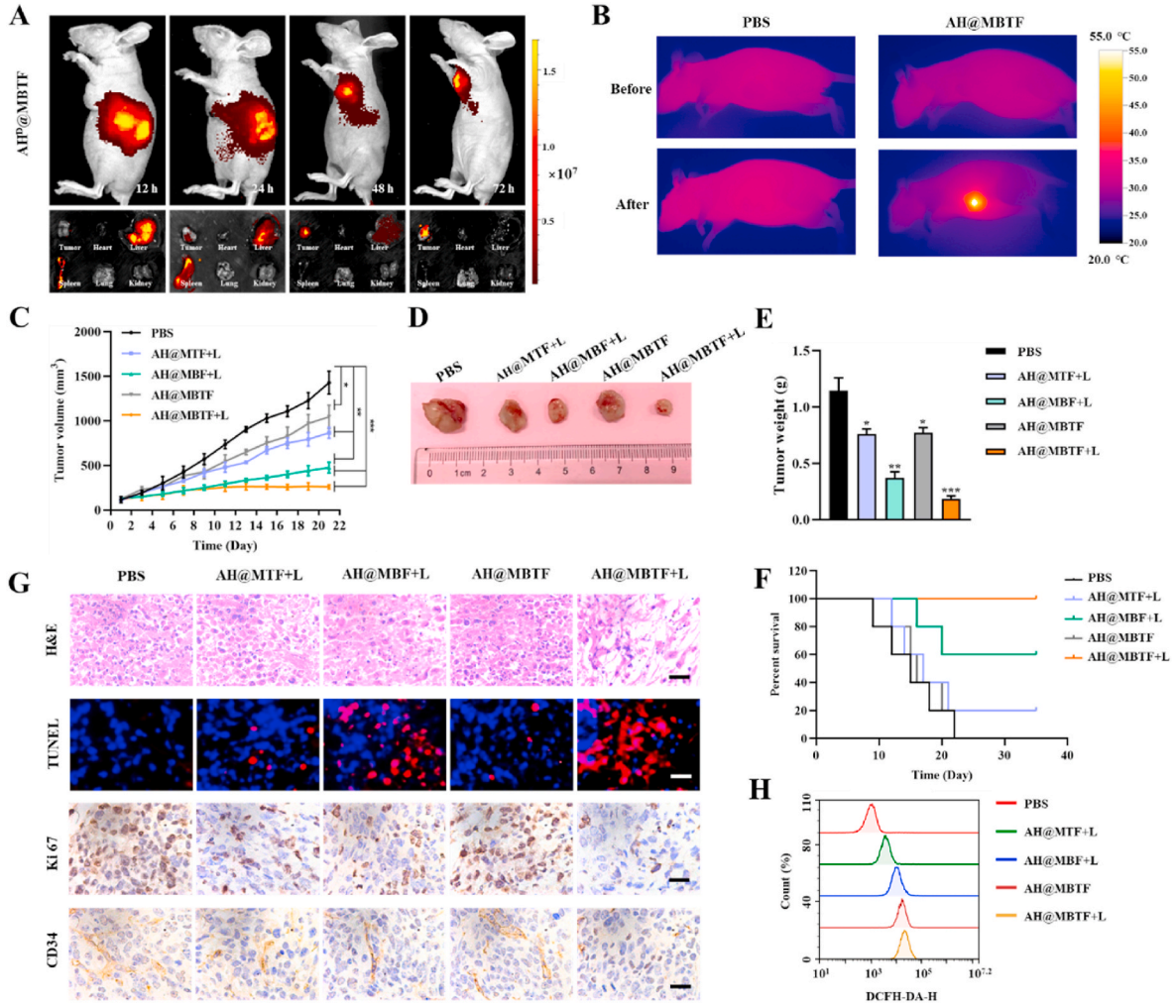

Fig. 5. A) Distribution of AH^{D}@MBTF *in vivo* at different time points and the fluorescence imaging of isolated organs and tumor. B) *in vivo* photothermal images of mice treated with PBS and AH@MBTF before and after laser irradiation. C) the growth curves of tumor volumes from tumor-bearing mice in different treatments: PBS, AH@MTF+L, AH@MBF+L, AH@MBTF, and AH@MBTF+L. D) The representative tumor images of various formulations at the 21st day. E) The quantitative statistics of tumor weight from different groups. F) The survival percentages of the tumor-bearing mice in 35 days. G) the ROS level of tumor tissues at the 21st day. H) H&E, TUNEL, Ki67, and CD34 staining of tumor tissues from different groups after 21 days therapies. AH^{D}@MTF+L represents the $ABTS^{DiR-HRP}$@MSN-TPP/FA; AH@MTF+L represents the $ABTS^{HRP}$@MSN-TPP/FA with 808 nm laser irradiation; AH@MBF+L represents the $ABTS^{HRP}$@MSN-BTU/FA with 808 nm laser irradiation; AH@MBTF represents the $ABTS^{HRP}$@MSN-BTU/TPP/FA; AH@MBTF+L represents the $ABTS^{HRP}$@MSN-BTU/TPP/FA with 808 nm laser irradiation. The scale bar is 100 μm $^{*}p < 0.05$, $^{**}p < 0.01$ and $^{***}p < 0.001$ versus PBS group.

AH@MBTF+L (copper-depleting therapy, photothermal therapy, chemo-dynamic therapy, and mitochondrial targeting). During the 21-day treatment period, the body weight of mice kept stable and even slightly increased, demonstrating that the nanoreactor did not cause severe systemic toxicity (Fig. S14). It can be seen from Fig. 5C that the tumor growth in AH@MTF+L and AH@MBTF was suppressed to a certain extent in contrast to PBS group. The tumor inhibition was further promoted by the combination therapy of copper-depleting therapy, photothermal therapy, and chemo-dynamic therapy (AH@MBF+L). With the assistant of TPP to target tumor mitochondria, the tumor volume in AH@MBTF+L was almost at a stagnant state after a brief rise, indicating the extraordinary antitumor activity that benefited from the significant synergistic effect. Moreover, the representative image of tumor tissues (Fig. 5D) and tumor weight (Fig. 5E) after 21 days of treatment were consistent with the result of tumor volume. In addition, the tumor inhibition rates of virous treatment groups were further calculated. As shown in Fig. S15, the tumor inhibition rates of single photothermal therapy group (AH@MTF+L) and single chemodynamic therapy group (AH@MBTF) were respectively 42.3 % and 30.12 %, even the sum of these values was far less than the inhibition rate of dual functional group (AH@MBTF+L, 89.03 %). The superiority of combination therapy could be attributed to the significant promotion of Fenton-like reaction by the rising temperature to produce more •OHFig. S12 [41,49,50] and the additional enhancement of photothermal therapy through the reduction in heat resistance of tumor cells caused by the generated •OH [51,52]. The results indicated that our nanoreactor exhibited the excellent collaborative treatments of photothermal therapy and chemodynamic therapy. According to the Kaplan–Meier plots of tumor-bearing mice (Fig. 5F), the final treatment group (AH@MBTF+L) markedly prolonged the survival rate of mice to 100 %. Then, the ROS generation in tumor sites was measured by flow cytometry to estimate the antitumor process. Evidently, the mice treated with AH@MBTF generated a large amount of ROS, while the laser radiation (AH@MBTF+L) further enhanced the formation of ROS (Fig. 5G). The quantitative analysis revealed that the accumulated ROS in the AH@MBTF+L treated mice was much higher than that of control group (Fig. S16). Then, the VEGF level of tumor tissue after various treatments was further tested. As can be seen from Fig. S17, the AH@MBTF treatment obviously inhibited the expression of VEGF. The inhibition effect of AH@MBTF+L to VEGF could be further enhanced by

the additional NIR irradiation, which could be attributed to the heat promoted copper capture [41] and the direct reduction of VEGF production caused by the photothermal mediated damage of tumor cells [53].

Upon the termination of antitumor experiment, the therapeutic effect of nanoreactor was further estimated by the H&E (analysis of tissue structure), TUNEL (characterizing apoptotic cells), Ki67 (typical marker of tumor proliferation), and CD34 (vascular endothelial cell marker) staining (Fig. 5H). The tumor tissue treated with AH@MBTF+L presented remarkable cell necrosis and nuclear rupture, massive apoptotic cells (red fluorescence), down-regulation of Ki67 expression, and reduction of CD34 marker. These results further demonstrated that the AH@MBTF+L could inhibit tumor growth, induce tumor cells apoptosis, suppress tumor proliferation, and prevent tumor angiogenesis.

To further verify the biosafety of nanoreactor, the H&E staining of main organs was conducted. As shown in Fig. S18, the tissue structures of organs still maintained intact and the noticeable pathological damage wasn't found. Additionally, the spleen weight of all experimental groups was similar with PBS group, implying that no inflammatory lesions occurred (Fig. S19). Furthermore, the serum was acquired for blood biochemistry analysis at the endpoint of various treatments to investigate the biocompatibility. As can be seen from Fig. S20, there were no significant differences of the major blood biochemistry indexes between 4T1 tumor-bearing mice treated by PBS and different formulations,

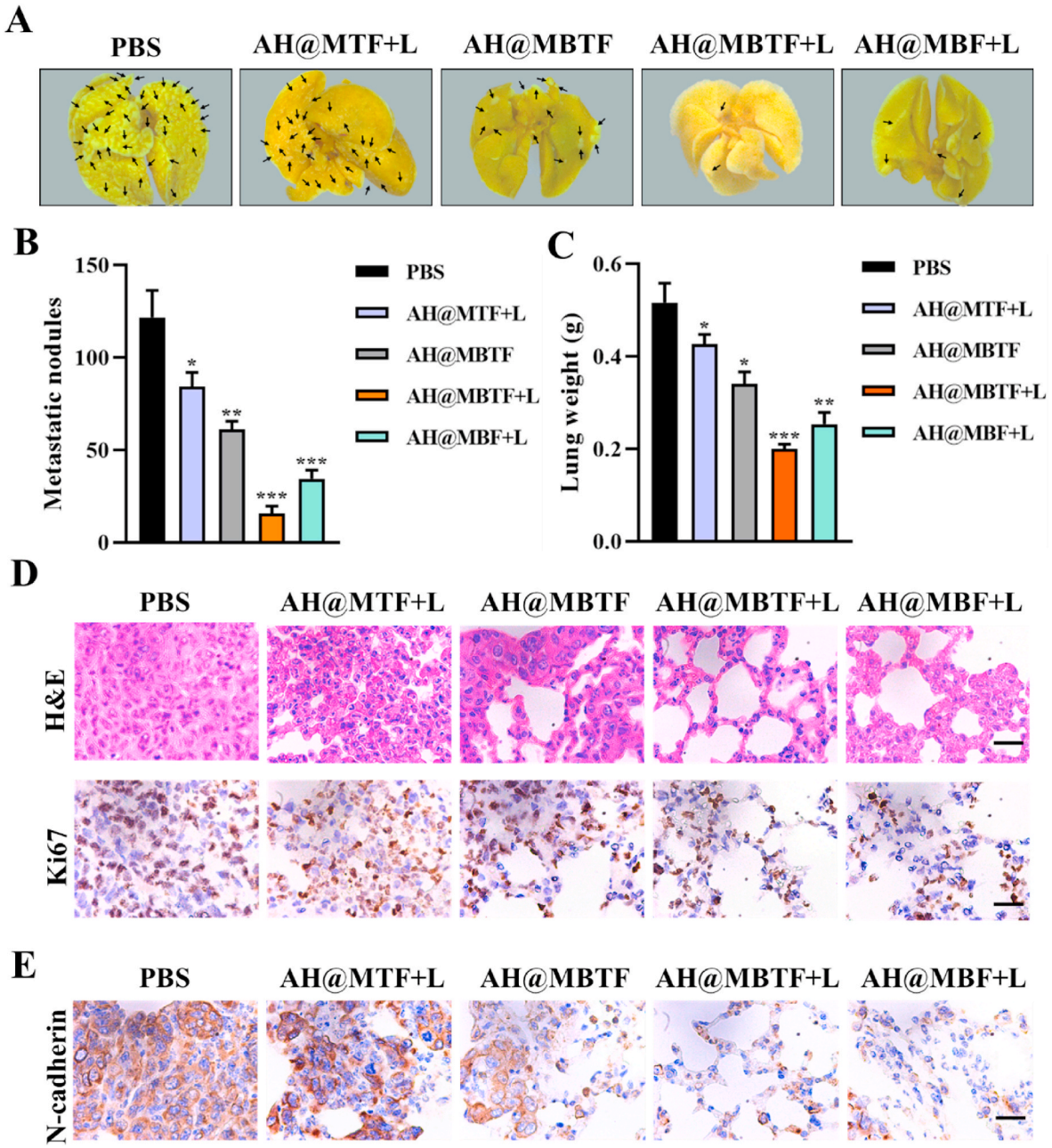

Fig. 6. A) Representative images of lung tissues with tumor metastasis after 450treatment with different formulations. B) The counting of metastatic nodules in the lung after various treatments. C) The weight statistics of lung tissues harvested from different groups. D) H&E and Ki 67 staining of the lung tissue after different treatments. E) Immunohistochemistry staining of N-cadherin (related transfer protein) with different formulations. AH@MTF+L represents the $ABTS^{HRP}$@MSN-TPP/FA with 808 nm laser irradiation; AH@MBF+L represents the $ABTS^{HRP}$@MSN-BTU/FA with 808 nm laser irradiation; AH@MBTF represents the $ABTS^{HRP}$@MSN-BTU/TPP/FA; AH@MBTF+L represents the $ABTS^{HRP}$@MSN-BTU/TPP/FA with 808 nm laser irradiation. The scale bar is 50 μm $^{*}p < 0.05$, $^{**}p < 0.01$, and $^{***}p < 0.001$ versus PBS group.

indicating the high biocompatibility of our nanoreactor for tumor therapy. Therefore, it could be concluded that the AH@MBTF nanoreactor displayed considerably high safety *in vivo*.

3.5. In vivo anti-metastatic evaluation of AH@MBTF

As to the anti-metastatic property of AH@MBTF, an animal experiment was performed by utilizing the highly metastatic 4T1 breast cancer cells [54] At first, the 4T1 cells were subcutaneously injected into the right flank of mice (2×10^6 cells per mouse) to generate the primary tumor. After the tumor tissue grew to a proper size, the mice were intravenously injected with 4T1 cells suspension (1×10^5 cells per mouse) to simulate the tumor metastasis. Therefore, this established animal model contained both primary tumors and metastatic tumors. The treatment outcomes of primary tumors have been presented in the above chapter. The metastasis inhibition effect of nanoreactor *in vivo* was investigated and the lung tissues of these tumor-bearing mice were collected at the end of treatment. Subsequently, the isolated lungs were immersed in Bouin's fluid to form yellow metastatic nodules (Fig. 6A). Compared with the diffuse distribution of nodules in PBS, the metastatic foci substantially reduced through the treatment of AH@MBTF+L. Besides, the number of nodules was more than 120 in PBS group, while this number decreased down to about 15 with AH@MBTF+L treatment, confirming the inspiring anti-metastasis effect of synergistic strategy (Fig. 6B). The lung weight of mice treated with AH@MBTF+L dropped to normal level, signifying that the lung lesions were greatly alleviated (Fig. 6C). The pathological analysis suggested that the structure of lung tissue still maintained normal morphology and the proliferation of tumor was effectively inhibited in the AH@MBTF+L treated mice (Fig. 6D). Moreover, the down-regulation of transfer protein (N-cadherin) in AH@MBTF+L group further indicated the distinguished performance of metastasis suppression (Fig. 6E).

4. Conclusion

In summary, we reported a multifunctional nanoreactor (AH@MBTF) that can elicit superior anti-tumor and anti-metastasis effects based on capper depletion and H_2O_2-responsive photothermal-chemodynamic therapy. The nanoreactor apparently blocked tumor metastasis, which arose from the exhaustion of elevated copper in tumor. The complexation between BTU and copper ion involved the reduction from Cu^{2+} to Cu^{+}, catalyzing H_2O_2 to produce cytotoxic •OH, further promoting severe mitochondrial dysfunction. The synergistic effect of FA and TPP assisted nanoreactor to accurately accumulate in tumor mitochondria, where contained the rather high concentration of H_2O_2. It has been demonstrated that the loaded HRP catalyzed the conversion of ABTS to ABTS•$^{+}$, triggering H_2O_2-dependent photothermal therapy. Both *in vitro* and *in vivo* studies revealed that the nanoreactor formulation not only arrested primary tumor growth and prolonged survival period of tumor-bearing mice though raising local temperature and forming •OH, but also utilized copper deficiency to hinder tumor metastasis. All in all, the intelligent nanoreactor provided a novel inspiration in cancer treatment.

CRediT authorship contribution statement

Jie Liu: Data curation, Investigation, Writing – original draft. **Tianfeng Yang:** Data curation, Investigation. **Handan Zhang:** Formal analysis. **Lin Weng:** Formal analysis. **Xiuhong Peng:** Investigation. **Tao Liu:** Investigation, Writing – review & editing. **Cheng Cheng:** Formal analysis, Investigation. **Yanmin Zhang:** Supervision, Writing – review & editing. **Xin Chen:** Conceptualization, Funding acquisition, Supervision, Writing – review & editing.

Declaration of competing interest

The authors declare that they have no competing interests.

Acknowledgements

This work was supported by the National High Level Talents Special Support Plan (X.C.), the National Natural Science Foundation of China (82272141 to X.C.), the "Young Talent Support Plan" of Xi'an Jiaotong University (X.C.), the Shaanxi Innovative Research Team of Science and Technology (S2023-ZC-TD-0152), the Natural Science Foundation of Shaanxi Province (2022JZ-48 to X.C.), the National Key Research and Development Program of China (2023YFC2509104 to X.C.), and the Postdoctoral Science Foundation of China (2023M732812 to T.L.).

Appendix A. Supplementary data

Supplementary data to this article can be found online at https://doi.org/10.1016/j.bioactmat.2023.12.028.

References

[1] P. Sharma, M. Otto, Multifunctional nanocomposites modulating the tumor microenvironment for enhanced cancer immunotherapy, Bioact. Mater. 31 (2023) 440–462.
[2] N.M. Anderson, M.C. Simon, The tumor microenvironment, Curr. Biol. 30 (16) (2020) R921–R925.
[3] F.R. Balkwill, M. Capasso, T. Hagemann, The tumor microenvironment at a glance, J. Cell Sci. 125 (23) (2012) 5591–5596.
[4] E. Boedtkjer, S.F. Pedersen, The acidic tumor microenvironment as a driver of cancer, in: M.T. Nelson, K. Walsh (Eds.), Annual Review of Physiology, vol. 82, 2020, pp. 103–126.
[5] L. Bejarano, M.J.C. Jordao, J.A. Joyce, Therapeutic targeting of the tumor microenvironment, Cancer Discov. 11 (4) (2021) 933–959.
[6] Y. Liu, P. Bhattarai, Z. Dai, X. Chen, Photothermal therapy and photoacoustic imaging via nanotheranostics in fighting cancer, Chem. Soc. Rev. 48 (7) (2019) 2053–2108.
[7] S. Liu, X. Pan, H. Liu, Two-dimensional nanomaterials for photothermal therapy, Angew. Chem.-Int. Edit. 59 (15) (2020) 5890–5900.
[8] N. Fernandes, C.F. Rodrigues, A.F. Moreira, I.J. Correia, Overview of the application of inorganic nanomaterials in cancer photothermal therapy, Biomater. Sci. 8 (11) (2020) 2990–3020.
[9] H.S. Jung, P. Verwilst, A. Sharma, J. Shin, J.L. Sessler, J.S. Kim, Organic molecule-based photothermal agents: an expanding photothermal therapy universe, Chem. Soc. Rev. 47 (7) (2018) 2280–2297.
[10] L. Zou, H. Wang, B. He, L. Zeng, T. Tan, H. Cao, X. He, Z. Zhang, S. Guo, Y. Li, Current approaches of photothermal therapy in treating cancer metastasis with nanotherapeutics, Theranostics 6 (6) (2016) 762–772.
[11] H. Wang, J. Chang, M. Shi, W. Pan, N. Li, B. Tang, A dual-targeted organic photothermal agent for enhanced photothermal therapy, Angew. Chem.-Int. Edit. 58 (4) (2019) 1057–1061.
[12] A.C.V. Doughty, A.R. Hoover, E. Layton, C.K. Murray, E.W. Howard, W.R. Chen, Nanomaterial applications in photothermal therapy for cancer, Materials 12 (5) (2019).
[13] Z. Jiang, Z. Jiang, Y. Jiang, Y. Cheng, Q. Yao, R. Chen, L. Kou, Fe-involved nanostructures act as photothermal transduction agents in cancer photothermal therapy, Colloids Surf. B Biointerfaces 228 (2023).
[14] B. Yang, Y. Chen, J. Shi, Reactive oxygen species (ROS)-Based nanomedicine, Chem. Rev. 119 (8) (2019) 4881–4985.
[15] X. Xu, P.E. Saw, W. Tao, Y. Li, X. Ji, S. Bhasin, Y. Liu, D. Ayyash, J. Rasmussen, M. Huo, J. Shi, O.C. Farokhzad, ROS-responsive polyprodrug nanoparticles for triggered drug delivery and effective cancer therapy, Adv. Mater. 29 (33) (2017).
[16] Z. Zhou, H. Wu, R. Yang, A. Xu, Q. Zhang, J. Dong, C. Qian, M. Sun, GSH depletion liposome adjuvant for augmenting the photothermal immunotherapy of breast cancer, Sci. Adv. 6 (36) (2020).
[17] W. Yang, X. Shi, Y. Shi, D. Yao, S. Chen, X. Zhou, B. Zhang, Beyond the roles in biomimetic chemistry: an insight into the intrinsic catalytic activity of an enzyme for tumor-selective phototheranostics, ACS Nano 12 (12) (2018) 12169–12180.
[18] Q. Chen, C. Liang, X. Sun, J. Chen, Z. Yang, H. Zhao, L. Feng, Z. Liu, H(2)O(2)-responsive liposomal nanoprobe for photoacoustic inflammation imaging and tumor theranostics via in vivo chromogenic assay, Proc. Natl. Acad. Sci. U.S.A. 114 (21) (2017) 5343–5348.
[19] X. Guan, Cancer metastases: challenges and opportunities, Acta Pharm. Sin. B 5 (5) (2015) 402–418.
[20] D. Denoyer, S. Masaldan, S. La Fontaine, M.A. Cater, Targeting copper in cancer therapy: 'Copper that Cancer', Metallomics 7 (11) (2015) 1459–1476.
[21] E.C. de Heer, M. Jalving, A.L. Harris, HIFs, angiogenesis, and metabolism: elusive enemies in breast cancer, J. Clin. Invest. 130 (10) (2020) 5074–5087.

[22] W. Pi, L. Wu, J. Lu, X. Lin, X. Huang, Z. Wang, Z. Yuan, H. Qiu, J. Zhang, H. Lei, P. Wang, A metal ions-mediated natural small molecules carrier-free injectable hydrogel achieving laser-mediated photo-Fenton-like anticancer therapy by synergy apoptosis/cuproptosis/anti-inflammation, Bioact. Mater. 29 (2023) 98–115.
[23] C. Xu, Y. Kang, X. Dong, D. Jiang, M. Qi, Integration exosomes with MOF-modified multifunctional scaffold for accelerating vascularized bone regeneration, Chin. Chem. Lett. 34 (2) (2023).
[24] E.J. Ge, A.I. Bush, A. Casini, P.A. Cobine, J.R. Cross, G.M. DeNicola, Q.P. Dou, K. J. Franz, V.M. Gohil, S. Gupta, S.G. Kaler, S. Lutsenko, V. Mittal, M.J. Petris, R. Polishchuk, M. Ralle, M.L. Schilsky, N.K. Tonks, L.T. Vahdat, L. Van Aelst, D. Xi, P. Yuan, D.C. Brady, C.J. Chang, Connecting copper and cancer: from transition metal signalling to metalloplasia, Nat. Rev. Cancer 22 (2) (2022) 102–113.
[25] S. Shao, J. Si, Y. Shen, Copper as the target for anticancer nanomedicine, Adv. Ther. 2 (5) (2019).
[26] P. Zhou, J. Qin, C. Zhou, G. Wan, Y. Liu, M. Zhang, X. Yang, N. Zhang, Y. Wang, Multifunctional nanoparticles based on a polymeric copper chelator for combination treatment of metastatic breast cancer, Biomaterials 195 (2019) 86–99.
[27] S. Shao, Q. Zhou, J. Si, J. Tang, X. Liu, M. Wang, J. Gao, K. Wang, R. Xu, Y. Shen, A non-cytotoxic dendrimer with innate and potent anticancer and anti-metastatic activities, Nat. Biomed. Eng. 1 (9) (2017) 745–757.
[28] X. Chang, X. Tang, J. Liu, Z. Zhu, W. Mu, W. Tang, Y. Zhang, X. Chen, Precise starving therapy via physiologically dependent photothermal conversion promoted mitochondrial calcification based on multi-functional gold nanoparticles for effective tumor treatment, Adv. Funct. Mater. (2023) 2303596.
[29] H. Tian, M. Zhang, G. Jin, Y. Jiang, Y. Luan, Cu-MOF chemodynamic nanoplatform via modulating glutathione and H2O2 in tumor microenvironment for amplified cancer therapy, J. Colloid Interface Sci. 587 (2021) 358–366.
[30] D. Zhang, R. Xu, S. Chen, H. Du, S. Qian, F. Peng, X. Liu, Surface defect engineered-Mg-based implants enable the dual functions of superhydrophobic and synergetic photothermal/chemodynamic therapy, Bioact. Mater. 30 (2023) 15–28.
[31] H. Wang, X. Chang, Q. Ma, B. Sun, H. Li, J. Zhou, Y. Hu, X. Yang, J. Li, X. Chen, J. Song, Bioinspired drug-delivery system emulating the natural bone healing cascade for diabetic periodontal bone regeneration, Bioact. Mater. 21 (2023) 324–339.
[32] J. Xu, F. Zeng, H. Wu, S. Wu, A mitochondrial-targeting and NO-based anticancer nanosystem with enhanced photo-controllability and low dark-toxicity, J. Mater. Chem. B 3 (24) (2015) 4904–4912.
[33] J. Xu, F. Zeng, H. Wu, C. Hu, C. Yu, S. Wu, Preparation of a mitochondria-targeted and NO-releasing nanoplatform and its enhanced pro-apoptotic effect on cancer cells, Small 10 (18) (2014) 3750–3760.
[34] Z. Zeng, Y. Luo, X. Xu, T. Shan, M. Chen, Z. Huang, Y. Huang, C. Zhao, A mitochondria-targeting ROS-activated nanoprodrug for self-augmented antitumor oxidation therapy, J. Contr. Release 359 (2023) 415–427.
[35] L. Bao, G. Dou, R. Tian, Y. Lv, F. Ding, S. Liu, R. Zhao, L. Zhao, J. Zhou, L. Weng, Y. Dong, B. Li, S. Liu, X. Chen, Y. Jin, Engineered neutrophil apoptotic bodies ameliorate myocardial infarction by promoting macrophage efferocytosis and inflammation resolution, Bioact. Mater. 9 (2022) 183–197.
[36] T. Liu, M. Zhu, X. Chang, X. Tang, P. Yuan, R. Tian, Z. Zhu, Y. Zhang, X. Chen, Tumor-specific photothermal-therapy-assisted immunomodulation via multiresponsive adjuvant nanoparticles, Adv. Mater. 35 (18) (2023) e2300086.
[37] J. Saldana, P. Gallay, S. Gutierrez, M. Eguilaz, G. Rivas, Multi-walled carbon nanotubes functionalized with bathocuproinedisulfonic acid: analytical applications for the quantification of Cu(II), Anal. Bioanal. Chem. 412 (21) (2020) 5089–5096.
[38] C. Campos, R. Guzman, E. Lopez-Fernandez, A. Casado, Evaluation of the copper (II) reduction assay using bathocuproinedisulfonic acid disodium salt for the total antioxidant capacity assessment: the CUPRAC-BCS assay, Anal. Biochem. 392 (1) (2009) 37–44.
[39] L. Chen, T. Yang, L. Weng, X. Chang, J. Liu, X. Peng, C. Cheng, P. Han, Y. Zhang, X. Chen, Integration of tumor elimination and tissue regeneration via selective manipulation of physiological microenvironments based on intelligent nanocomposite hydrogel for postoperative treatment of malignant melanoma, Adv. Funct. Mater. (2023) 2304394.
[40] T. Yin, T. Yang, L. Chen, R. Tian, C. Cheng, L. Weng, Y. Zhang, X. Chen, Intelligent gold nanoparticles for malignant tumor treatment via spontaneous copper manipulation and on-demand photothermal therapy based on copper induced click chemistry, Acta Biomater. 166 (2023) 485–495.
[41] X. Chang, M. Zhu, X. Tang, X. Yu, F. Liu, L. Chen, T. Yin, Z. Zhu, Y. Zhang, X. Chen, Enhanced manipulation of tumor microenvironments by nanomotor for synergistic therapy of malignant tumor, Biomaterials 290 (2022) 121853.
[42] S. Lamouille, J. Xu, R. Derynck, Molecular mechanisms of epithelial-mesenchymal transition, Nat. Rev. Mol. Cell Biol. 15 (3) (2014) 178–196.
[43] X. Chang, Z. Zhu, L. Weng, X. Tang, T. Liu, M. Zhu, J. Liu, W. Tang, Y. Zhang, X. Chen, Selective manipulation of the mitochondria oxidative stress in different cells using intelligent mesoporous silica nanoparticles to activate on-demand immunotherapy for cancer treatment, Small (2023) 2307310.
[44] A. Aranda, L. Sequedo, L. Tolosa, G. Quintas, E. Burello, J.V. Castell, L. Gombau, Dichloro-dihydro-fluorescein diacetate (DCFH-DA) assay: a quantitative method for oxidative stress assessment of nanoparticle-treated cells, Toxicol. Vitro 27 (2) (2013) 954–963.
[45] J. Liu, Y. Jin, Z. Song, L. Xu, Y. Yang, X. Zhao, B. Wang, W. Liu, K. Zhang, Z. Zhang, J. Shi, Boosting tumor treatment by dredging the hurdles of chemodynamic therapy synergistic ion therapy, Chem. Eng. J. 411 (2021) 128440.
[46] J. Zhao, Y. Chen, T. Xiong, S. Han, C. Li, Y. He, Y. He, G. Zhao, T. Wang, L. Wang, T. Cheng, C. Wang, J. Wang, Clustered cobalt nanodots initiate ferroptosis by upregulating heme oxygenase 1 for radiotherapy sensitization, Small 19 (10) (2023) 2206415.
[47] Z.-Z. Dong, C. Yang, Z. Wang, Z. Zhong, M.-S. Wong, H.-W. Li, Tumor microenvironment-responsive Zn/Cu nanoparticles for enhanced chemodynamic therapy, Smart Mater. Med. 4 (2023) 286–293.
[48] S. Sakamuru, M.S. Attene-Ramos, M. Xia, Mitochondrial membrane potential assay, in: H. Zhu, M. Xia (Eds.), High-Throughput Screening Assays in Toxicology, 2016, pp. 17–22.
[49] P. Yuan, G. Dou, T. Liu, X. Guo, Y. Bai, D. Chu, S. Liu, X. Chen, Y. Jin, On-demand manipulation of tumorigenic microenvironments by nano-modulator for synergistic tumor therapy, Biomaterials 275 (2021) 120956.
[50] L. Chen, T. Yang, R. Tian, T. Yin, L. Weng, Y. Bai, Y. Zhang, X. Chen, Near-infrared and tumor environment Co-activated nanoplatform for precise tumor therapy in multiple models, Appl. Mater. Today 24 (2021) 101133.
[51] X. Ding, T. Wang, S. Bai, M. Yang, N. Peng, T. Qiu, Y. Liu, A dual heat shock protein down-regulation strategy using PDA/Cu/ICG/R controlled by NIR “switch” enhances mild-photothermal therapy effect, Adv. Healthcare Mater. 12 (27) (2023) 101133.
[52] J. Ma, N. Li, J. Wang, Z. Liu, Y. Han, Y. Zeng, In vivo synergistic tumor therapies based on copper sulfide photothermal therapeutic nanoplatforms, Explorations 3 (5) (2023) 20220161.
[53] X. Dai, X. Li, Y. Du, M. Han, Z. Wang, Y. Wang, F. Yan, Y. Liu, Gold Nanorod-mesoporous silica core shell nanocomposites for NIR-II photothermal ablation and dual PD-L1/VEGF blockade therapy in hepatocellular carcinoma, Chem. Eng. J. 459 (2023) 141426.